Newcastle University

Newcastle University ePrints

Patrício SG, Papaioannou E, Zhang G, Metcalfe IS, Marques FMB. High performance composite CO_2 separation membranes. *Journal of Membrane Science* 2014, 471, 211–218.

Copyright:

©2014 Elsevier B.V

NOTICE: this is the author's version of a work that was accepted for publication in *Journal of Membrane Science.* Changes resulting from the publishing process, such as peer review, editing, corrections, structural formatting, and other quality control mechanisms may not be reflected in this document. Changes may have been made to this work since it was submitted for publication. A definitive version was subsequently published in *Journal of Membrane Science*, Volume 471, 2014, DOI Link: http://dx.doi.org/10.1016/j.memsci.2014.08.007

Further information on publisher website: www.elsevier.com

Date deposited: 27-10-2014

Version of file: Author Final Version

This work is licensed under a Creative Commons Attribution-NonCommercial 3.0 Unported License

ePrints – Newcastle University ePrints
http://eprint.ncl.ac.uk

High Performance Composite CO_2 Separation Membranes

S.G. Patrício[a], E. Papaioannou[b], G. Zhang[b], I.S. Metcalfe[b], F.M.B. Marques[a]

[a]Dept. of Materials and Ceramic Eng./CICECO, University of Aveiro

3810-193 Aveiro, Portugal

[b]School of Chemical Eng. and Advanced Materials, Newcastle University

Merz Court, Newcastle upon Tyne NE1 7RU, UK

Abstract

The CO_2 permeation of composite membranes obtained by impregnation of molten alkaline carbonates into a Gd-doped ceria ceramic skeleton was tested using several gas mixtures with up to 50 vol% CO_2 as feed gas and Ar in the membrane permeate side. Experiments performed in the 550-850 °C temperature range showed high permeation rates reaching 0.6 $ml.min^{-1}.cm^{-2}$ at 850 °C for the higher CO_2 content. These values exceed those often reported for similar membranes and conditions. Furthermore, the characterization of the ceramic skeletons and composite membranes by impedance spectroscopy (in air at low temperature) could be used to estimate the temperature where dual oxide and carbonate ionic transport are balanced (around 800 °C). The inherent shift in the CO_2 permeation activation energy is shown to match closely this prediction.

Keywords:

CO_2 permeation; impedance spectroscopy, composite electrolytes; ceria; molten carbonates

***Corresponding author:**

fmarques@ua.pt, tel: +351234370269, fax: +351234370204

1. Introduction

While renewable energy technologies continuously grow and mature, the present energy supply scenario still relies to a large extent on fossil fuels. In order to reduce the negative environmental consequences of the inherent high CO_2 emissions, technologies for the separation of this gas are urgently needed. In the combustion of fossil fuels the flue gas is often at relatively high temperature and includes a high CO_2 content combined with water vapor. Similarly, in the water-gas shift reaction used after the partial oxidation of methane to produce hydrogen, CO_2 is again available at high temperature. Separation techniques able to handle such gas streams without cooling are obviously interesting in different applications [1, 2].

In recent years, composite oxide and salt CO_2 separation membranes were suggested and tested with promising results [3-12]. The basic idea is that the combination of an oxide-ion conductor (usually a ceria-based electrolyte as those used in Solid Oxide Fuel Cells-SOFCs) with a carbonate-ion conductor (alkaline carbonate mixtures as used in Molten Carbonate Fuel Cells-MCFCs) provides net CO_2 transport if both ions move in opposite directions within the membrane. Considering this mechanism, these membranes should be fully selective, unlike earlier concepts where electronic conductors were combined with carbonate-ion conductors, providing mixed CO_2 and O_2 transport [13].

The exact operating mechanism of these composite CO_2 separation membranes is still under debate. Molten alkaline carbonates are complex systems including a wide range of stable ionic species [14]. Possible coupling of movements of distinct species in opposite directions, like the previously mentioned simple combination of carbonate and oxide ions, is one of the obvious possibilities. However, combined movement of alkaline ions and alkaline carbonate molecules is also able to yield net carbonate-ion transport [15]. Considering the wide range of species present, the variety of possible effects due to distinct groupings of species is enormous, as suggested schematically in Table 1. Furthermore, the membrane selectivity might be lost in the presence of significant electronic conductivity via the molten carbonates [15], in line with the no selectivity when using mixed carbonate and metal composite membranes [13].

While the design of ideal composite membranes should be feasible combining the established knowledge on MCFC and SOFC technologies, the situation is by far more complex since the functional role of the ceramic phase in the separation membranes is more demanding than in MCFCs. In fact, in an efficient composite membrane the net transport rates of both ionic species must be balanced. Since typical alkaline carbonate mixtures above their melting point (around 500 °C) reach extremely high ionic conductivities (»0.1 $S.cm^{-1}$ [16, 17]), the ceramic

electrolytes are probably the rate limiting element. In fact, such high oxide-ion conductivities can only be reached at 800 °C in standard dense ceria-based electrolytes [18, 19]. Also, alternative ceramic electrolytes show poor chemical stability in the presence of molten carbonates preventing their utilization in this type of systems [20, 21].

In composite membranes the ceramic phase must be porous to act as a sponge with respect to the molten carbonates. This means that the effective conductivity of the porous ceramic is even lower than for the corresponding dense oxide. Furthermore, grain boundaries in ceramics are known for their oxide-ion blocking characteristics. Thus, the percolation model between ceramic grains, obvious pathway for oxide-ions, must be optimized. These aspects emphasize the importance of the ceramic microstructure on the composite membrane performance. Other approaches to improve the overall membrane performance involve the manipulation of the membrane thickness (thin substrate supported membranes), since the ionic conductance is thickness dependent. This approach has been tested with good results [6, 7, 12].

In any concept, to try to circumvent the disparate ionic conductivities of the membrane phase constituents the easiest solution is to unbalance their relative volume proportions or move to high temperature. The latter solution must take into consideration the limited long term stability of molten carbonates at high temperature. Thus, tuning the ceramic microstructure to avoid as much as possible inevitable interfacial and constriction resistances is mandatory.

Recently we have shown that we can tune the microstructure and monitor the effectiveness of adopted solutions using impedance spectroscopy at low temperature, well below the target membrane operating conditions. At temperatures around 300 °C, impedance spectroscopy provides enough information on the ceramic skeleton even when an impregnated membrane is tested [20, 22-24]. The membranes' performance at low temperature is governed by the most conductive ceramic phase, a situation that is reversed above the carbonates' melting temperature. Interestingly, modeling previously published on composite membrane performance is rich in microstructural parameters describing relevant issues like the ionic pathway tortuosity and volume fraction of each phase, but there has been no attempt to really investigate the role the ceramic backbone "electrical microstructure". This is more complex in nature than the result of a direct combination of microstructural parameters. Impedance spectroscopy is the obvious tool to access this information in a simple manner and could provide sound supporting information for microstructural design.

Following promising signs on operational membrane microstructural characteristics obtained as previously described [20, 22-24], we now include membrane characterization through CO_2 permeation measurements. The consistency and comparative analysis of data now presented

with previously published results confirm the relevance of an optimized ceramic skeleton and the efficacy of the suggested testing procedure.

2. Experimental

Composites hereby studied were based on CGO ($Ce_{0.9}Gd_{0.1}O_{1.95}$, from Praxair, with an average particle size in the order of 120 nm), known oxide-ion conductor. A set of samples was prepared with initial consolidation of the ceramic skeleton followed by impregnation with molten carbonates. The CGO powder was firstly coarsened by calcination (1 h) at 1500 °C, and afterwards mildly milled with 0.5 wt% PVA (polyvinyl alcohol) to aid the forming process. Powders were uniaxially pressed (125 MPa) as disks with about 15×10^{-3} m diameter and 2×10^{-3} m thick and then submitted to isostatic pressure (200 MPa). Sintering of these substrates was also conducted at 1500 °C (4 h), after a binder burnout stage, which explains the abbreviation CGO1500 used throughout this work to designate these materials.

One eutectic mixture of sodium and lithium carbonates (Sigma-Aldrich, 48:52 molar ratio), hereby named NLC, was prepared by high energy milling in a planetary ball mill with Nylon containers and zirconia-based balls (balls to powder mass ratio of 10:1, respectively). Impregnation with the molten carbonates was performed at 700 °C during 90 min, under light vacuum (about 0.1 atm, manual control with a valve, manometer and water vacuum pump).

Bulk characteristics of all samples (densification of the ceramic skeleton, fraction of mixed carbonates inserted in the porous matrix, final densification of composites) were monitored to assess the reproducibility of the entire manufacturing process. The samples mass and dimensions were registered in every stage and their phase content estimated based on own or standard reference data for each constituent phase. To avoid irregular surface conditions, namely after impregnation, all samples were lightly polished before dimensional and gravimetric analysis.

A typical set of sample characteristics is shown in Table 1, including those used in this work either for electrical measurements and microstructural analysis (CGO1500A) or for CO_2 permeation experiments (CGO1500B and CGO1500C). In fact, the large sequence and number of measurements reported in the following paragraphs required repeated cycles of electrode deposition and removal (impedance spectroscopy and SEM/EDS before and after impregnation), also replacement of the membrane after detection of sealing problems in the permeation experiments. Furthermore, the potential diffusion of Au electrodes (used in impedance spectroscopy) to the composites interior might be influential in terms of CO_2

permeation and should be avoided using freshly impregnated samples. This explains the utilization of distinct samples for parallel characterization techniques and also the attention dedicated to the selection of close sample characteristics from a single batch, as those listed in Table 1.

The electrical performance of ceramic skeletons and composite membranes was evaluated by impedance spectroscopy (HP 4284A LCR Meter) using a test ac signal amplitude of 0.5 V (lower values were occasionally applied to identify the electrode contributions) within the 20 Hz to 1 MHz frequency range (points logarithmically spaced with 10 readings per decade). These operating conditions were previously validated using distinct signal amplitudes [30]. Prior to the electrical measurements, samples were painted with Au paste. These electrodes were fired in air at 600 ºC for 20 min. These cells were afterwards placed in a spring loaded cell holder where gold wires are used as current collectors, with all measurements performed in air within the temperature range 200 to 700 ºC. The spectra were analyzed with ZView v3.0 (Scribner), including fitting to equivalent circuits. Microstructural characterization was performed by scanning electron microscopy (SEM, Hitachi SU-70) coupled with one energy dispersive X-ray detector (EDS, Bruker Quantax 400).

For the high temperature carbon dioxide permeation experiments a dual chamber permeation setup was used operated at atmospheric pressure. The volumes of the feed-side and permeate-side chambers were 11.5 cm^3 and 250 cm^3 respectively. The membrane was mounted on the top of an alumina tube demarcating the two chambers using a high temperature commercial silver sealant (Fuel Cell Materials, silver ink AG-1, 73.8% wt). The sealant was allowed to dry in air for 12 hours at 75 °C before firing under oxidizing conditions at around 750 °C to sinter and remove the organic constituents. The final active membrane area available for permeation was approximately 5×10^{-5} m^2. The gases used, provided by BOC (certified gases, compositions on a molar basis), were 50% CO_2/50% N_2 (Cylinder C-1) and pure Ar (Cylinder C-2). During the permeation experiments the feed side inlet was composed of a mixture of the gases from C-1 and C-2 in such a way that the carbon dioxide mole fraction was from 10% up to 50%. C-2 gas was used as inlet for the permeate side feed. Nitrogen in C-1 was used as a means to indicate inter-chamber leaks and in particular was chosen to be of a similar mole fraction to that of carbon dioxide in C-1 in order to estimate any carbon dioxide leak rates. The flows on both the feed and permeate sides were maintained at 20 cm^3 (STP)/min. The outlet feed-side and permeate-side gases were analysed using two identical mass spectrometers (HIDEN, HALO 100-RC) which were calibrated before the experiment. For permeation experiments the membrane was heated in a temperature programmable furnace (VECSTAR VCTF-1) up to every operating temperature (from 550 °C to 850 °C) at 120 °C h^{-1}. At each temperature the mole fraction of carbon dioxide was varied

from 10% up to 50%. After the end of the experiment the membrane was carefully removed from the alumina tube and placed in a desiccator to avoid hydration. To determine the fluxes the permeate-side outlet mole fraction is multiplied by the molar flow rate on the permeate side, $\dot{n}''$, and divided by the active area of the membrane, A (5×10^{-5} m^2)

$$\text{Flux} = \left[\{x''_{CO_2}(outlet)\}\dot{n}''\right]A^{-1}$$

where x''_{CO_2} is the carbon dioxide mole fraction and '' refers to the permeate side. Permeances are calculated by dividing the flux by the carbon dioxide partial pressure driving force while permeabilities are calculated by multiplying permeances by the membrane thickness, of about 10^{-3} m.

Post-operation analysis of samples used in permeation experiments included Raman spectroscopy (Bruker RFS 100/S using the 1064 nm light wavelength provided by a Nd:YAG laser) and combined SEM/EDS analysis. This set of analyses tried to elucidate the nature and potential impact of a black film observed in one single case on the composite membrane feed side surface.

3. Results and Discussion

3.1. Microstructural characterization

SEM micrographs of CGO1500 skeletons and CGO1500-based composite membranes are shown in Figures 1A and B, respectively. In Figure 1A the skeleton voids between ceramic blocks appear as dark areas. Further attention to the microstructural characteristics of the ceramic phase (light grey) shows that these large blocks consist of tiny and densely sintered ceramic grains. This is the result of the powder coarsening step adopted to manipulate the packing mode of the green ceramic when shaped by pressing. In Figure 1B the voids already appear clearly filled with a second phase, the mixed carbonates.

In Figure 1C we present the composite atomic number map distributions with emphasis on Ce and Na, the easily detected dominant constituents of each phase. Light Li is outside the element range capability of EDS. Apparent Gd spots might indicate slight lixiviation of this element from CGO but it is also known that Gd tends to segregate at the surface of CGO [25, 26]. Fast mass diffusion through the molten carbonates phase might favor the agglomeration of this constituent in localized areas, maybe as constituent of a minor secondary phase. In fact, previous long-term tests with similar composites (up to 1000 h performed in air and in CO_2 at 550 °C) provided no evidence for degradation of the ceramic phase or the composite

[27]. However, direct assessments of the reactivity of rare-earth oxides with alkaline carbonates within an extended range of temperatures showed a significant difference between CeO_2 (quite inert) and Gd_2O_3 (reactive) [28, 29]. This means that the apparent presence of Gd spots, although believed here as having no major relevance on performance, should be considered in further detail after membrane endurance tests, to confirm (or not) selective lixiviation of this dopant from the oxide phase, with impact on the oxide-ion transport within the ceramic.

Besides those details just discussed, Figure 1C mostly shows the presence of interconnected “pools” of carbonates (green) between percolating regions where the ceramic phase (red) prevails. Overall, these microstructures confirm that the processing route is able to provide dense composite membranes from porous ceramics by impregnation with molten carbonates.

3.2. Impedance spectroscopy

Figures 2A and B include the impedance spectra of the porous CGO1500A substrate and corresponding composite, in air, at 250 and 600 °C. These two extreme temperatures were selected for being representative of conditions where the carbonates are solid or liquid, respectively. Distinct contributions at high frequency (HF), intermediate frequency (IF), and low frequency (LF, electrode tail) can easily be discerned at lower temperatures based on a systematic study of the roles of ac sign magnitude and dc bias on the actual shape of these spectra. Since the impedance spectra of porous substrates is significantly influenced by microstructural characteristics, and the situation is even more complex when in the presence of a composite, we intentionally avoid here a direct identification of (HF and IF) impedance arcs with bulk grain and grain boundary performance. In previous work we have addressed in detail all these aspects and also the role of the nature and content of the ceramic phase on the impedance of these composites providing the necessary background for the present analysis [20, 22-24, 30].

The high temperature spectra of skeleton and composite are distinct in shape but mostly in magnitude (Figure 2B) consisting only of the usually named electrode arc, extending to negative -Z” values due to the setup inductance. In fact, at high temperature we can only assess the total conductivities of porous and impregnated membranes from the high frequency intercept with the Z’ axis. The small impedance of the composite with respect to the skeleton is easily understood since we are above the carbonates eutectic temperature and in such conditions they have much higher conductivity than the ceramic phase. This also confirms that the molten carbonates clearly percolate throughout the entire membrane thickness and that parallel electrical contributions of both phases can be assumed at least as a simplified composite description.

At low temperature (Figure 2A) data confirms the close relation between the electrical properties of the porous skeleton and those of the composite membrane, with the HF and IF arcs appearing as fingerprint of the ceramic phase, preserved even after impregnation with the carbonates. We should emphasize here that these data were actually obtained with the same sample, before and after impregnation with the mixed alkaline carbonates. Looking qualitatively at the rationale for this ceramic fingerprint in both spectra, we must recall that the ceramic phase is the most conductive in this temperature range, thus determining the composite conductivity. The resistive alkaline carbonates act here as a parallel “inactive” high impedance pathway.

The low temperature spectra can be easily deconvoluted into two main HF and IF contributions corresponding to two elementary circuits in series, each consisting of a parallel R||CPE arrangement, where R stands for a resistor and CPE for a constant phase element. A detailed discussion on this type of procedure and also limitations can be found elsewhere [22, 23].

Microstructural analysis in addition to the high and low temperature impedance measurements reported here confirm that both phases percolate throughout the composite, providing parallel electrical pathways for distinct charge carriers. Furthermore, since the HF and IF contributions in fact reflect the (dc) oxide-ion transport through the ceramic skeleton, including bulk, grain boundary, porosity and constriction resistance effects, the total HF+IF arc magnitudes and their temperature dependencies can be used to optimize/scrutinize the microstructural characteristics of these substrates. This procedure supported the present choice of CGO1500 as permeation membrane [24].

Extrapolation of these data to high temperature and comparison against the composite total conductance can also be used to try to predict the conditions where the conductance of both phases is roughly balanced, corresponding to ideal operating conditions. This argument is illustrated in Figure 3, including several sets of values of conductivity and conductance. Open symbols correspond to actual measurements while lines correspond mostly to extrapolated tendencies from low temperature values, below the temperature range used in this figure ($T>500$ °C or $1000/T< 1.3$ K^{-1}).

In Figure 3 the first thing we should notice is that the conductivity of the mixed carbonates above melting (σ_{NLC}) is higher than the composites conductivity ($\sigma_{composite}$). A simple mixture law can explain this based on the lower conductivity of the ceramic phase in this range, however dominant in volume fraction (Table 1). Nevertheless, since the skeleton conductivity ($\sigma_{skeleton}$) shows higher activation energy than the composite, on increasing the membrane

working temperature we reach the point where the ionic transport via each phase should match. This number is pinpointed in the conductance lines as $T_{working}$ (in the present case $T_{working}$~775 °C, $1000/T_{working}$~0.95 K^{-1}). Based on the above mentioned estimates, this is the temperature where the CGO skeleton conductance (G_{CGO}) becomes half the total composite conductance ($G_{composite}$), following the assumed parallel contributions of individual phases to the composite conductance. One last aspect that should be noticed is that the CGO skeleton IF conductance (G_{interf}, strongly dependent on microstructure) at this temperature easily exceeds the HF conductance but is still significant.

The present extrapolation of results obtained in air to a situation where the cell is under a CO_2 gradient has a somewhat limited efficacy since we are dealing with distinct atmospheres. However, at high temperature there is only a slight difference in the conductivity of these composites on changing from air to CO_2 [31]. So, the central reasoning just presented is essentially valid as guidance.

3.3. CO_2 permeation

Figure 4 presents the carbon dioxide flux (J_{CO_2}) through the membranes as a function of temperature, for different CO_2 partial pressures (CGO1500B used for 10-40 vol% CO_2 and CGO1500C for 50 vol% CO_2). Permeation rates increase with the mole fraction of CO_2 in the membrane feed side and also with temperature, as expected. Higher mole fraction of CO_2 in the feed side increases the thermodynamic driving force for permeation and increasing temperature facilitates the ionic transport of ionic species involved.

One first aspect deserving attention is on the relative magnitudes of permeation rates compared to those mentioned in the literature. For comparable types of membranes and working conditions the present results exhibit fluxes that exceed all those previously reported (Table 2) although Zhang et al. [12] and Dong et al. [4] appear to have achieved higher fluxes by employing a solid oxide porous matrix with highly inter-connected pores and an asymmetric tubular structure, respectively. Recently Norton et al. [33] also achieved higher fluxes and enhanced membrane stability by introduction of oxygen in the feed gas due to a change in transport mechanism in the membrane.

We must emphasize here that the membrane permeation is dependent on thickness and feed and permeate side gas phase composition. For that reason we calculate the permeability of our membrane accounting for the carbon dioxide driving force along with the thickness of the membrane and compare the result with the literature. Carbon dioxide permeability was measured ~4.05×10^{-11} mol m^{-1} s^{-1} Pa^{-1}, at 650 ^{o}C and reached ~$8.46\ 10^{-11}$ mol m^{-1} s^{-1} Pa^{-1} at 850 ^{o}C. M. Zuo et al. [6] used a YSZ-carbonate hollow fibre dual phase membrane which

exhibited carbon dioxide permeabilities of 4.5×10^{-14} and 9.6×10^{-14} mol $m^{-1} s^{-1} Pa^{-1}$ at 650 ^{o}C and 850 ^{o}C, respectively (values estimated from Fig. 7(I) based on experimental details). A CGO-carbonate dual phase membrane was prepared by Wade et al. [11]; carbon dioxide permeabilities of 8×10^{-13} mol $m^{-1} s^{-1} Pa^{-1}$ at 650 ^{o}C and up to 5×10^{-12} mol $m^{-1} s^{-1} Pa^{-1}$ at 850 ^{o}C were measured. The same group also produced YSZ-carbonate membranes with carbon dioxide permeabilities as high as 8×10^{-12} mol $m^{-1} s^{-1} Pa^{-1}$ at 850 ^{o}C [11]. A comparison of our results with the above work [6, 11] indicate that the carbon dioxide permeability of the CGO-carbonate membrane developed in this study is higher than that reported for YSZ- and CGO-carbonate membranes operated at similar temperatures and under similar operational conditions. Also, since the effective permeation flux should increase decreasing the membrane thickness, assuming that the permeation is governed by bulk dual ionic transport, this means that the present good performance still shows room for improvement on moving to substrate supported thin membranes, following the positive results already obtained with such concepts (Table 2).

Secondly, from impedance spectroscopy data we were able to estimate a temperature where oxide-ion transport starts prevailing with respect to carbonate-ion transport. Since on increasing the temperature the overall flux should move from oxide to carbonate-ion governed, it seems tempting a comparison of activation energies (E_a) for the total flux with those obtained for the ionic conductivity of each phase and composite. The relevant Arrhenius-type plots are presented in Figure 4B, including the corresponding E_a values. Consistently, the permeation activation energy decreases on increasing the temperature, starting at low temperature with values around 70-80 kJ/mol (typical of oxide-ion transport governed kinetics) and moving to values in the order of 40-50 kJ/mol at higher temperature, closer to typical values found for the molten alkaline carbonates which are of the order of 20 kJ/mol [16-17]. Furthermore, the predicted shift in rate determining regime around 1000/T=0.95 K^{-1} is consistent with the data in Figure 4B. In fact, while in this figure the apparent break in activation energy seems to be around 1000/T=1.05 K^{-1}, we must recall that the reported 40-50 kJ/mol activation energies are still well above the expected values when permeability is controlled by the carbonate conductivity. We are likely in a regime of mixed kinetic control. This means that the actual breaking point in activation energies should be found at higher temperatures (lower 1000/T values) in Figure 4B, consistent with the prediction from impedance data. This is a remarkable result since direct extrapolation from low temperature (around 200-350 °C) to high temperature has significant constraints, primarily due to the limited temperature range available and for being unable to fully account for the usual bending observed in Arrhenius-type plots of ionic conductivity versus temperature.

In Figure 5 we present the results of combined SEM/EDS analysis of the membrane feed side after being tested in permeation experiments, when the feed gas stream was changed from diluted carbon dioxide to argon while cooling the membrane. The reason for this specific inspection was the appearance of a black deposit on this feed side as opposed to the normal lighter appearance similar to the permeate side. Also, since two pellets were used in the permeation experiment, this blackening was only present when the feed gas was changed to Ar on cooling. In the samples cooled in diluted carbon dioxide there was no evidence for this effect. Lastly, the surrounding tubes in the setup also showed no evidence for such blackening.

Since the reported effect seemed a carbon deposit, a standard SEM/EDS analysis was performed but without the deposition of any carbon or alternative conducting film. The easy observation of this sample by SEM in such conditions together with the clear homogeneity of the carbon coverage confirmed the initial assumption (Figure 5). Carbon is obviously present in the carbonates but the C and Na atomic number maps coverage in the observed surface are totally distinct. Na is localized while C spreads all over the surface. Also, Raman spectroscopy (Figure 6) showed a clear fingerprint of the presence of carbon with a broad band at 1575 cm^{-1} and a shoulder around 1325 cm^{-1} commonly assigned as G and D bands of carbon vibrations modes, respectively [34]. This spectrum is clearly distinct from that obtained for a fresh composite membrane surface, showing the intense stretching vibration bands of Li_2CO_3 and Na_2CO_3 at 1075 and 1090 cm^{-1} [35]. Furthermore, the weak bands in the range 1385-1585 cm^{-1} also related with carbonate stretching vibrations [36] are quite different from those observed in the CO_2 exposed membrane surface.

The source of carbon must be the CO_2 stream. The well-known formation of carbon from disproportionation of CO might occur if the CO_2 stream is partly reduced. A slight uptake of oxygen by lightly reduced CGO and/or mixed conduction through the composite membrane under specific working conditions might drive this partial reduction. Interestingly, the potential in-situ coverage of the membrane feed side with a thin electronic conducting film should show a positive role on the membrane performance due to the delocalization of the feed-side surface reactions. In fact, the composite membrane concept relies on the localized formation of carbonate ions at the surface of the membrane from reaction between CO_2 molecules and oxide-ions from the ceramic phase. As such, we need the carbonates, the oxide and the gas in close vicinity. With some electronic conductivity at the membrane feed-side surface, this reaction can be split into the delocalized formation of oxygen atoms and/or molecules at the gas/oxide/electronic conductor triple phase contacts with ulterior diffusion and reduction elsewhere for combination with CO_2 molecules to form carbonate ions.

One comment is needed on the actual surface reaction kinetics and ionic species involved in the bulk transport. The present knowledge on the kinetics of MCFCs electrode processes suggests that we should take into consideration a larger number of species present in the system (e.g., peroxide, superoxide and dicarbonate ions [37-38]). This means that the present understanding of the surface kinetics of membrane performance is certainly limited. Also, recent questioning on the exact relevance of alkaline ions on the ionic transport in molten carbonates (presumably underestimated in most cases), supported in alkaline metal and carbon diffusion experiments performed in the past, should be considered with great care [15, 40]. In fact, early literature on MCFCs claimed that alkaline and carbonate ions showed close values of diffusion coefficients (same order of magnitude), even the same activation energies, although totally distinct from the actual electrical conductivity activation energy observed for the salts (by a factor of 3-4 in solid state, still a factor of 2 when molten [17, 41-43]). Furthermore, recent modelling suggests that these species might be bonded in multiple types of "anchored" ions like $NaCO_3^-$ or $LiCO_3^-$, more stable than isolated Na^+, Li^+, or CO_3^{2-} ions [14]. This type of reasoning is very much in line with the idea that in molten salts we have the same neighbourhoods as in solids but no long distance order [42].

Also, the potential stability of these membranes must be tested as a function of temperature and surrounding atmospheres. However, the known long term stability of commercial MCFC and the reported results on the stability of these composite electrolytes at temperatures close to those used in this work [27-44], all seem promising. Furthermore, the present concept is versatile enough to operate already at about 500-550 °C, obviously with lower performance, even so with room for improvement based on alternative cell concepts. These aspects emphasize the enormous room for research on actual ionic transport mechanisms and optimization of these membranes for target applications.

4. Conclusions

Composite CO_2 separation membranes with one of the highest permeation rates ever reported were successfully prepared based on microstructurally tailored ceria-based pre-sintered skeletons impregnated with molten alkaline carbonates. The strong relationship found by impedance spectroscopy between the performances of the ceramic phase alone and after impregnation could be used to predict the temperature range where the membrane CO_2 permeation regime changed from oxide-ion to carbonate-ion controlled. This prediction was found to be consistent with the temperature dependence of permeation data.

Acknowledgement

The research leading to these results has received funding from the European Research Council under the European Union's Seventh Framework Programme (FP/2007-2013) / ERC Grant Agreement Number 320725, from the EPSRC via a PLATFORM Grant, EP/G012865/1, also from FEDER via COMPETE and national funding (Portugal) by FCT, through the project CICECO - FCOMP-01-0124-FEDER-037271 (FCT PEst-C/CTM/LA0011/2013). S. Patrício thanks FCT for the post-doctoral grant (BPD/75943/2011).

5. References

[1] P. Luis, T. Van Gerven, B. Van der Bruggen, Recent developments in membrane-based technologies for CO_2 capture, Prog. Energ. Combust., 38 (2012) 419-448.
[2] K. Sugiura, K. Takei, K. Tanimoto, Y. Miyazaki, The carbon dioxide concentrator by using MCFC, J. Power Sources, 118 (2003) 218-227.
[3] M. Anderson, Y.S. Lin, Carbonate-ceramic dual-phase membrane for carbon dioxide separation, J. Membr. Sci., 357 (2010) 122-129.
[4] X.L. Dong, J.O. Landeros, Y.S. Lin, An asymmetric tubular ceramic-carbonate dual phase membrane for high temperature CO_2 separation, Chem. Comm., 49 (2013) 9654-9656.
[5] Y.D. Li, Z.B. Rui, C. Xia, M. Anderson, Y.S. Lin, Performance of ionic-conducting ceramic/carbonate composite material as solid oxide fuel cell electrolyte and CO_2 permeation membrane, Catal. Today, 148 (2009) 303-309.
[6] M. Zuo, S.Zuo, X.Y. Tan, B. Meng, N.T. Yang, S.M. Liu, Ionic conducting ceramic–carbonate dual phase hollow fibre membranes for high temperature carbon dioxide separation, J. Membr. Sci, 458 (2014) 58-65.
[7] J. Ortiz-Landeros, T. Norton, Y.S. Lin, Effects of support pore structure on carbon dioxide permeation of ceramic-carbonate dual-phase membranes, Chem.l Eng. Sci., 104 (2013) 891-898.
[8] Z.B. Rui, M. Anderson, Y.D. Li, Y.S. Lin, Ionic conducting ceramic and carbonate dual phase membranes for carbon dioxide separation, J. Membr. Sci., 417 (2012) 174-182.
[9] Z.B. Rui, M. Anderson, Y.S. Lin, Y.D. Li, Modeling and analysis of carbon dioxide permeation through ceramic-carbonate dual-phase membranes, J. Membr. Sci., 345 (2009) 110-118.
[10] J.L. Wade, K.S. Lackner, A.C. West, Transport model for a high temperature, mixed conducting CO_2 separation membrane, Solid State Ionics, 178 (2007) 1530-1540.
[11] J.L. Wade, C. Lee, A.C. West, K.S. Lackner, Composite electrolyte membranes for high temperature CO_2 separation, J. Membr. Sci., 369 (2011) 20-29.

[12] L.L. Zhang, N.S. Xu, X. Li, S.W. Wang, K. Huang, W.H. Harris, W.K.S. Chiu, High CO_2 permeation flux enabled by highly interconnected three-dimensional ionic channels in selective CO_2 separation membranes, Energ. Environ. Sci., 5 (2012) 8310-8317.
[13] S.J. Chung, J.H. Park, D. Li, J.I. Ida, I. Kumakiri, J.Y.S. Lin, Dual-phase metal-carbonate membrane for high-temperature carbon dioxide separation, Ind. Eng. Chem. Res., 44 (2005) 7999-8006.
[14] W.R. Carper, P.G. Wahlbeck and T.R. Griffiths, DFT Models of Molecular Species in Carbonate Molten Salts, J. Phys. Chem. B 116 (2012) 5559−5567.
[15] H. Näfe, Electrochemical CO_2 Separation through an Alkali-Carbonate-Based Membrane, ECS J. Solid State Sci. Tech., 3 (2014) N23-N29.
[16] T. Kojima, Y. Miyazaki, K. Nomura, K. Tanimoto, Electrical conductivity of molten Li_2CO_3-X_2CO_3 (X : Na, K, Rb, and Cs) and Na_2CO_3-Z_2CO_3 (Z : K, Rb, and Cs), J. Electrochem. Soc., 154 (2007) F222-F230.
[17] P.L. Spedding, Electrical Conductance of Molten Alkali Carbonate Binary-Mixtures, J. Electrochem. Soc., 120 (1973) 1049-1052.
[18] F.M.L. Figueiredo, F.M.B. Marques, Electrolytes for solid oxide fuel cells, WIREs, 2 (2013) 52-72.
[19] B.C.H. Steele, A. Heinzel, Materials for fuel-cell technologies, Nature, 414 (2001) 345-352.
[20] A.S.V. Ferreira, T. Saradha, F.L. Figueiredo, F.M.B. Marques, Compositional and microstructural effects in composite electrolytes for fuel cells, Int. J. Energ. Res., 35 (2011) 1090-1099.
[21] K. Pointon, B. Lakeman, J. Irvine, J. Bradley, S. Jain, The development of a carbon-air semi fuel cell, J. Power Sources, 162 (2006) 750-756.
[22] C.M.C. Soares, S.G. Patrício, F.M.L. Figueiredo, F.M.B. Marques, Relevance of the ceramic content on dual oxide and carbonate-ion transport in composite membranes, Int. J. Hydrogen Energ., 39 (2014) 5424-5432.
[23] A.I.B. Rondão, S.G. Patrício, F.M.L. Figueiredo, F.M.B. Marques, Impact of ceramic matrix functionality on composite electrolytes performance, Electrochim. Acta, 109 (2013) 701-709.
[24] S.G. Patrício, C.M.C. Soares, C.F.N. Santos, F.M.L. Figueiredo, F.M.B. Marques, Ceria-based substrates for CO_2 separation membranes, Solid State Ionics, 262 (2014) 248–252.
[25] E. Ruiz-Trejo, J.D.Sirman, Y.M. Baikov, J.A. Kilner, Oxygen ion diffusivity, surface exchange and ionic conductivity in single crystal Gadolinia doped Ceria, Solid State Ionics, 113-115 (1998) 565-569.

[26] P.J Scanlon, R.A.M.Bink, F.P.F. van Berkel, G.M. Christie, L.J. van IJzendoorn, H.H. Brongersma, R.G. van Welzenis, Surface composition of ceramic CeGd–oxide, Solid State Ionics, 112 (1998) 123-130.
[27] A.I.B. Rondão, S.G.Patrício, F.M.L. Figueiredo, F.M.B. Marques, Composite electrolytes for fuel cells: Long-term stability under variable atmosphere, Int. J. Hydrogen Energ., 39 (2014) 5460-5469.
[28] K.I. Ota, Y. Matsuda, K. Matsuzawa, S. Mitsushima, N. Kamiya, Effect of rare earth oxides for improvement of MCFC, J. Power Sources, 160 (2006) 811-815.
[29] M. Yamauchi, Y. Itagaki, H. Aono, Y. Sadaoka, Reactivity and stability of rare earth oxide-Li_2CO_3 mixtures, J. Eur. Ceram. Soc., 28 (2008) 27-34.
[30] A.S.V. Ferreira, C.M.C. Soares, F.M.H.L.R. Figueiredo, F.M.B. Marques, Intrinsic and extrinsic compositional effects in ceria/carbonate composite electrolytes for fuel cells, Int. J. Hydrogen Energ., 36 (2011) 3704-3711.
[31] A.I.B. Rondão, S.G. Patrício, F.M.L. Figueiredo, F.M.B. Marques, Role of gas-phase composition on the performance of ceria-based composite electrolytes, Int. J. Hydrogen Energ., 38 (2013) 5497 - 5506.
[32] B. Lu, Y.S. Lin, Synthesis and characterization of thin ceramic-carbonate dual-phase membranes for carbon dioxide separation, J. Membr. Sci., 444 (2013) 402-411.
[33] T.T. Norton, J. Ortiz-Landeros, Y.S. Lin, Stability of La-Sr-Co-Fe Oxide-Carbonate Dual-Phase Membranes for Carbon Dioxide Separation at High Temperatures, Ind. Eng. Chem. Res., 53 (2014) 2432-2440.
[34] A.C. Ferrari, J. Robertson, Interpretation of Raman spectra of disordered and amorphous carbon, Phys. Rev. B, 61 (2000) 14095-14107.
[35] M.H. Brooker, J.B. Bates, Raman and Infrared Spectral Studies of Anhydrous Li_2CO_3 and Na_2CO_3, J. Chem. Phys., 54 (1971) 4788-&.
[36] S. Kohara, N. Koura, Y. Idemoto, S. Takahashi, M.L. Saboungi, L.A. Curtiss, The structure of $LiKCO_3$ studied by ab initio calculations and Raman spectroscopy, J. Phys. Chem. Solids, 59 (1998) 1477-1485.
[37] R.W. Reeve, A.C.C. Tseung, Factors affecting the dissolution and reduction of oxygen in molten carbonate electrolytes. Part 1: Effect of temperature and alkali carbonate mixture, J. Electroanal. Chem. 403 (1996) 69-83.
[38] M. Cassir, G. Moutiers, J. Devynck, Stability and characterization of oxygen species in alkali molten-carbonate - a thermodynamic and electrochemical approach, J. Electrochem. Soc., 140 (1993) 3114-3123.
[39] L.J. Chen, C.J. Lin, J. Zuo, L.C. Song, C.M. Huang, First spectroscopic observation of peroxocarbonate/peroxodicarbonate in molten carbonate, J. Phys. Chem. B, 108 (2004) 7553-7556.

[40] H. Naefe, Conductivity of alkali carbonates, carbonate-based composite electrolytes and IT-SOFC, Ecs J. Solid State Sci. Tech., 3 (2014) N7-N14.
[41] R.L. Frederick, E.K. Williams, ^{22}Na and ^{14}C Diffusion in a Mixture of Li/Na/KCO_3, J. Electrochem. Soc., 116 (1969) 454-455.
[42] P.L. Spedding, R. Mills, Trace-Ion Diffusion in Molten Alkali Carbonates, J. Electrochem. Soc., 112 (1965) 594-599.
[43] P.L. Spedding, R. Mills, Tracer Diffusion Measurements in Mixtures of Molten Alkali Carbonates, J. Electrochem. Soc., 113 (1966) 599-603.
[44] K. Pointon, B. Lakeman, J. Irvine, J. Bradley, S. Jain, The development of a carbon–air semi fuel cell, J. Power Sources 162 (2006) 750–756

Table and figure captions

Table 1

Schematic description of possible coupling of movements of species yielding distinct types of net ionic and/or molecular transport

Table 2

Bulk characteristics of samples used in this study.

Table 3

Comparative analysis of data on CO_2 permeation.

Figure 1 - Microstructures of ceramic skeletons before (A) and after impregnation (B) at low magnification (1.5 k). For easier visualization of phase distribution in composite membranes, a combined atomic number map is also provided in (C).

Figure 2 - Impedance spectra at 250 (A) and 600 °C (B), in air, of CGO1500A ceramic skeletons and corresponding composite membranes. The inset in (A) shows an exploded view of high frequency data.

Figure 3 -.Electrical conductivity (σ) and conductance (G) Arrhenius-type plots of CGO skeletons (total and interfacial contributions) and composite membranes. Symbols correspond to actual measurements in this temperature range. Lines describe tendencies from own data, obtained from extrapolation of low temperature measurements. The conductivity for NLC estimated from the literature [17]. The meaning of the internal captions can be found in the main text.

Figure 4 - Carbon dioxide flux through the CGO1500B and CGO1500C composite membranes as a function of temperature, for different carbon dioxide partial pressures in the feed gas (A). In (B) Arrhenius-type plot of permeation fluxes for extreme CO_2 contents in the feed gas to highlight varying activation energies. Total gas flow rate: 20 ml (STP)/min.

Figure 5 - Microstructure (A), combined atomic number map (B) and separate carbon and sodium atomic number maps (C and D, respectively) of a membrane feed side after CO_2 permeation experiments, magnification 5.0 k (see text for details).

Figure 6 - Raman spectra of (a) freshly prepared dual-phase composite membranes and (b) from the membrane feed side surface after high-temperature permeation measurements.

Table 1

System	Moving species	Movement/species		Net forward ➔	Ref.
		forward ➔	reverse ➔		
Generic	AB, A	AB	A	B	
Composite oxide/molten carbonate ionic conductors	CO_3^{2-}, O^{2-}	CO_3^{2-}	O^{2-}	CO_2	[3-12]
Molten Na_2CO_3	Na_2CO_3, Na^+	Na_2CO_3	(2 x) Na^+	CO_3^{2-}	[15]
Molten Na_2CO_3 (examples of possible effects based on claimed species present)	$NaCO_3^-$, Na^+	$NaCO_3^-$	Na^+	CO_3^{2-}	[14]
	CO_4^{4-}, CO_3^{2-}	CO_4^{4-}	CO_3^{2-}	O^{2-}	

Table 2

Sample	Tests	Processing stage		
		Porous skeleton	Composite	
		Densification (%)[1]	Vol% of carbonates[2]	Densification (%)[3]
CGO1500A	Impedance spectroscopy and SEM/EDS	72	23	99
CGO1500B	Permeation up to 40 vol% CO_2	70	26	98
CGO1500C	Permeation with 50 vol% CO_2	73	21	98

[1] Based on the Archimedes method
[2] Based on mass balance before and after impregnation
[3] Based on total mass, phase composition and sample dimensions

Table 3

Oxide	vol%	T (°C)	Feed side vol% CO_2 (others)	Membrane type (thickness)			CO_2 permeation flux[2] ($ml.cm^{-2}.min^{-1}$)	Permeability[2] ($mol.m^{-1}.s^{-1}.Pa^{-1}$)	Ref.
				Geometry	Support[1]	Thickness (mm)			
YSZ	?	650	50 (N_2)	Hollow fibre	Substrate	thin	0.06	4.5×10^{-14}	[6]
YSZ	~55		25 (N_2)	Flat	Substrate	thin	0.52	7×10^{-13}	[32]
SDC/NiO	50		48 (5 H_2, N_2)	Flat	Self	1.2	1.35	2.7×10^{-10}	[12]
SDC/NiO	70		48 (5 H_2, N_2)	Flat	Self	1.2	0.10	2.1×10^{-11}	[12]
CGO	64		50 (He)	Flat	Self	0.2-0.4	0.013-0.025	8×10^{-13}	[11]
YSZ	66		50 (He)	Flat	Self	0.2-0.4	0.013-0.025	8×10^{-13}	[11]
CGO	73		50 (N_2)	Flat	Self	0.92	0.236	4.05×10^{-11}	This work
YSZ	?	850	50 (N_2)	Tubular	Substrate	thin	0.13	9.6×10^{-14}	[6]
SDC	>65		50 (N_2)	Tubular	Substrate	0.15	1.12	2.6×10^{-11}	[4]
SDC	65		50 (N_2)	Tubular	Self	1.5	0.32	8.2×10^{-11}	[4]
CGO	64		50 (He)	Flat	Self	0.2-0.4	0.15-0.32	5×10^{-12}	[11]
YSZ	66		50 (He)	Flat	Self	0.2-0.4	0.14-0.28	8×10^{-12}	[11]
CGO	73		50 (N_2)	Flat	Self	0.92	0.604	8.46×10^{-11}	This work

[1] Self-supported membrane or substrate supported

[2] Reported values or estimated from plots (occasionally assuming likely cell dimensions based on experimental details)

Figure 1

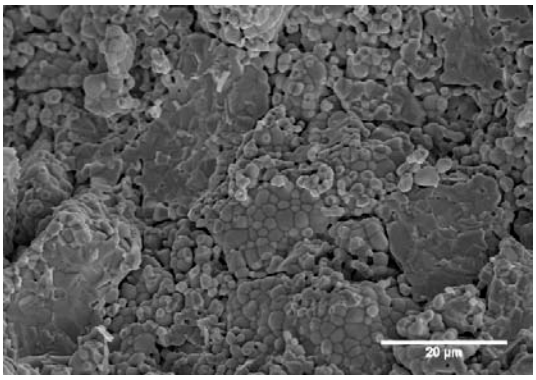

A

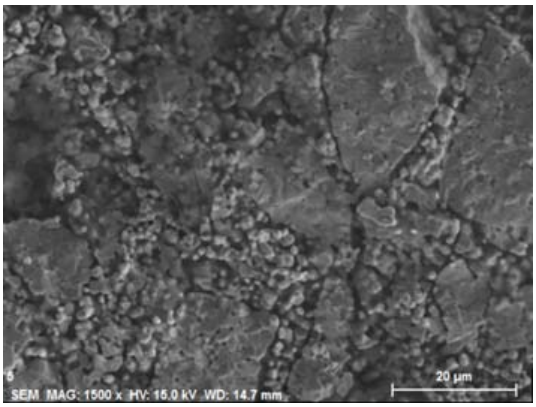

B

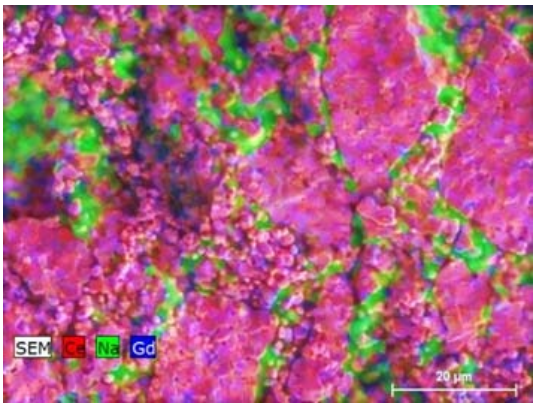

C

Figure 2

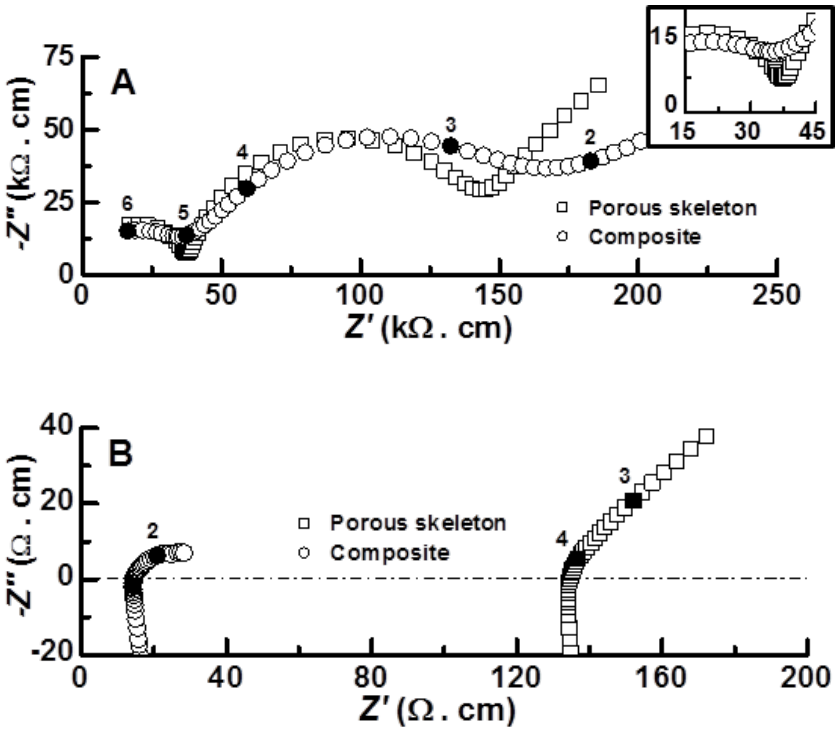
A
-Z'' (kΩ . cm)
Z' (kΩ . cm)
Porous skeleton
Composite
B
-Z'' (Ω . cm)
Z' (Ω . cm)
Porous skeleton
Composite

Figure 3

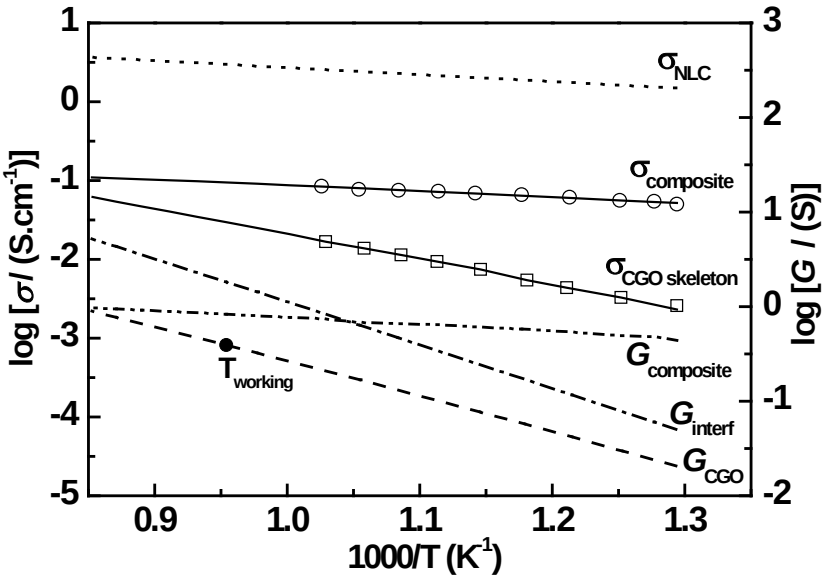
σNLC
σcomposite
σCGO skeleton
Gcomposite
Ginterf
GCGO
Tworking
log [σ / (S.cm-1)]
log [G / (S)]
1000/T (K-1)
1
0
-1
-2
-3
-4
-5
3
2
1
0
-1
-2
0.9
1.0
1.1
1.2
1.3

Figure 4

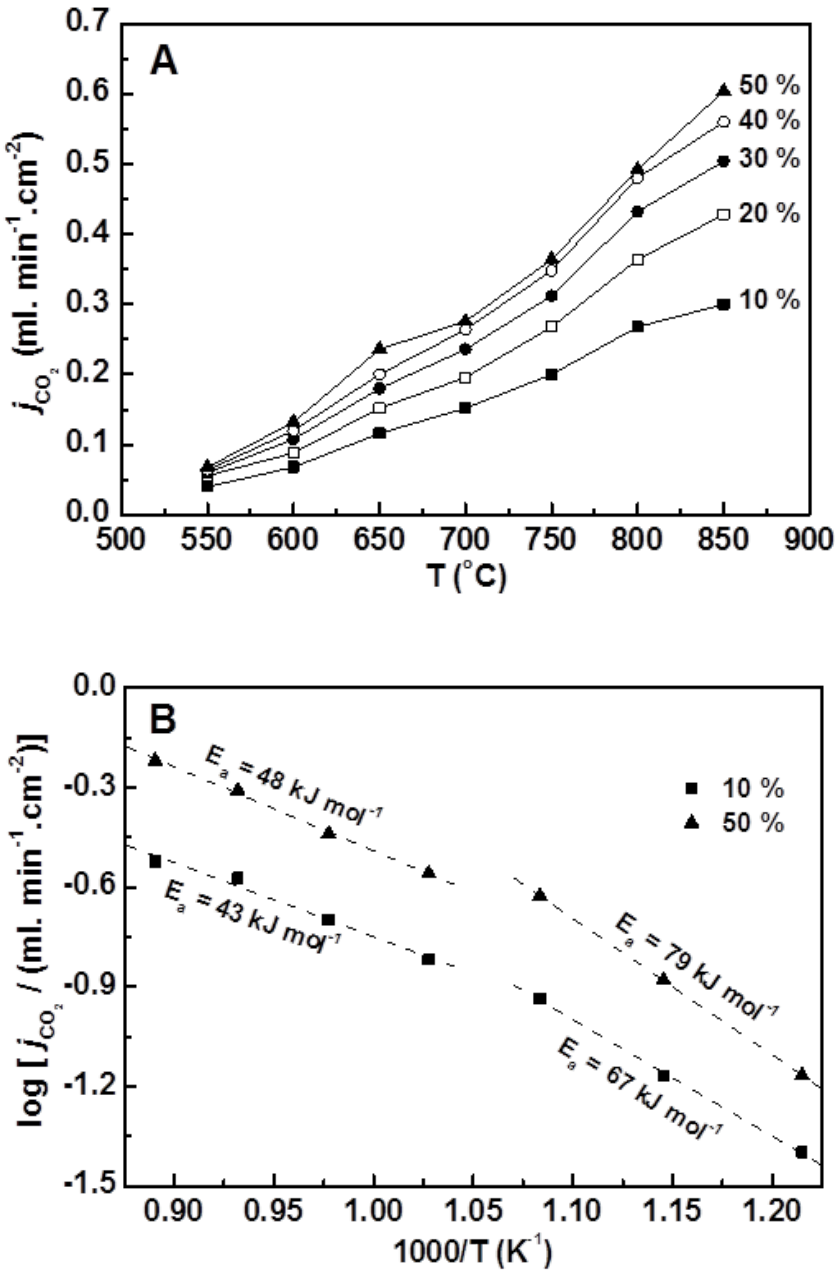
A
50 %
40 %
30 %
20 %
10 %
j_{CO_2} (ml. min^{-1}.cm^{-2})
T (°C)
B
10 %
50 %
E_a = 48 kJ mol^{-1}
E_a = 43 kJ mol^{-1}
E_a = 79 kJ mol^{-1}
E_a = 67 kJ mol^{-1}
log [j_{CO_2} / (ml. min^{-1}.cm^{-2})]
1000/T (K^{-1})

Figure 5

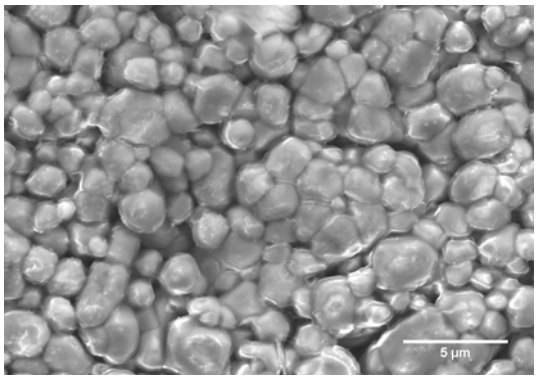

A

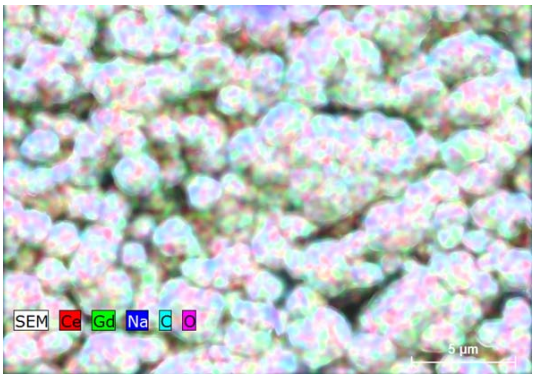

B

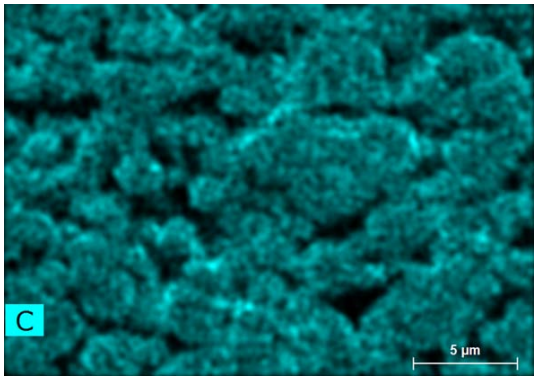

C

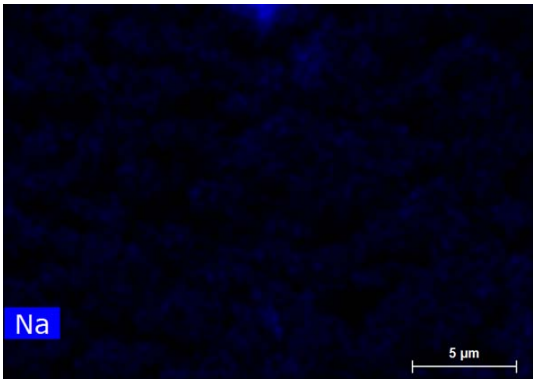

D

Figure 6

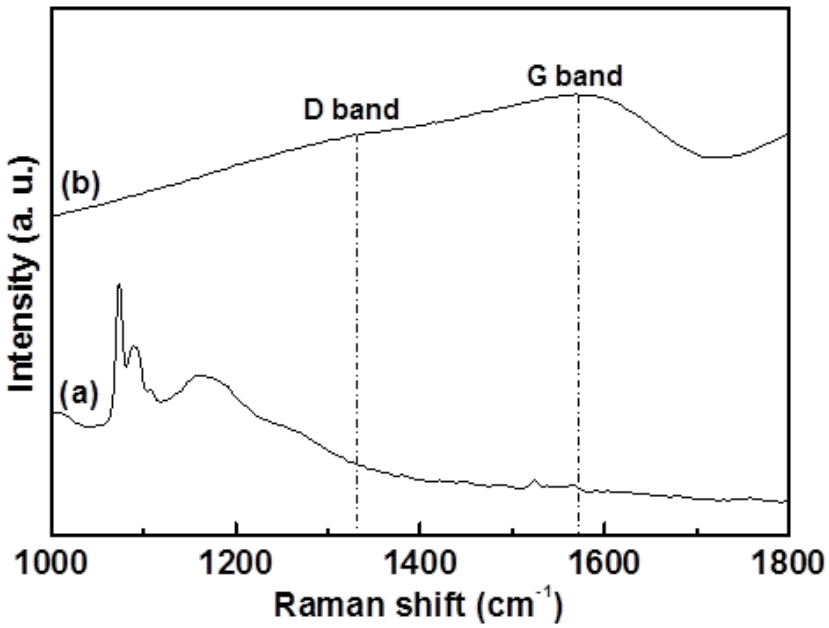
G band
D band
(b)
(a)
Intensity (a. u.)
1000
1200
1400
1600
1800
Raman shift (cm-1)